

# WSe<sub>2</sub> as Transparent Top Gate for Infrared Near-Field Microscopy

Niels C. H. Hesp, Mark Kamper Svendsen, Kenji Watanabe, Takashi Taniguchi, Kristian S. Thygesen, Iacopo Torre,\* and Frank H. L. Koppens\*



Cite This: *Nano Lett.* 2022, 22, 6200–6206



Read Online

ACCESS |



Metrics & More



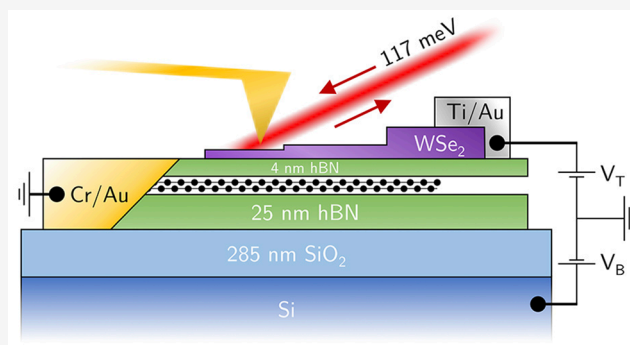
Article Recommendations



Supporting Information

**ABSTRACT:** Independent control of carrier density and out-of-plane displacement field is essential for accessing novel phenomena in two-dimensional (2D) material heterostructures. While this is achieved with independent top and bottom metallic gate electrodes in transport experiments, it remains a challenge for near-field optical studies as the top electrode interferes with the optical path. Here, we characterize the requirements for a material to be used as the top-gate electrode and demonstrate experimentally that few-layer WSe<sub>2</sub> can be used as a transparent, ambipolar top-gate electrode in infrared near-field microscopy. We carry out nanoimaging of plasmons in a bilayer graphene heterostructure tuning the plasmon wavelength using a trilayer WSe<sub>2</sub> gate, achieving a density modulation amplitude exceeding  $2 \times 10^{12} \text{ cm}^{-2}$ . The observed ambipolar gate–voltage response allows us to extract the energy gap of WSe<sub>2</sub>, yielding a value of 1.05 eV. Our results provide an additional tuning knob to cryogenic near-field experiments on emerging phenomena in 2D materials and moiré heterostructures.

**KEYWORDS:** near-field microscopy, top gate, transparent electrode, ambipolar, 2D materials



Near-field optical microscopy is a powerful technique for exploring the optical properties of materials on the nanoscale.<sup>1</sup> Scattering-type scanning near-field microscopy (s-SNOM) is the most commonly used type of near-field optical microscopy in the study of two-dimensional (2D) materials and their heterostructures. In this configuration, a sharp metallic tip (with a typical apex radius of  $\approx 20 \text{ nm}$ ) generates a hotspot of light that interacts with the sample. The tip also bridges the momentum mismatch between free-space light and collective excitations, like plasmon<sup>2,3</sup> or phonon polaritons,<sup>4,5</sup> making s-SNOM an appealing tool for imaging these excitations.<sup>6,7</sup> Importantly, in 2D materials it is possible to continuously tune the carrier density via the field effect, using a gate electrode underneath the sample. Notably, in single-layer graphene, tuning the carrier density has allowed for an understanding of the mechanism of photocurrent generation in near-field photocurrent experiments.<sup>8</sup> Moreover, the carrier density has a direct impact on the plasmon dispersion. Varying the carrier density in s-SNOM experiments on graphene plasmons<sup>2,3,9,10</sup> has given crucial information to understand the nature of these collective excitations, and the role of many-body effects.<sup>11</sup> Tuning the carrier density also gave an insight into the plasmonic properties of a photonic lattice formed by minimally twisted bilayer graphene.<sup>12</sup> The modulation of the carrier density can also be exploited to enhance the signal-to-noise ratio of the recorded signal via a lock-in detection

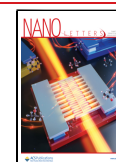
scheme. This technique was employed to detect intersubband transitions in transition metal dichalcogenides (TMDs).<sup>13</sup>

The application of a gate voltage on a sample has an additional consequence: Besides injecting carriers into the sample, it induces a perpendicular electric displacement field. While the effect of the displacement field on the properties of single-layer graphene is minor, it can have a more pronounced impact on multilayer materials. For instance, a displacement field leads to an opening of a band gap in bilayer graphene.<sup>14</sup> Hence, independent control of the carrier density and displacement field is of great relevance for exploring novel phenomena in 2D materials using s-SNOM. For example, the domain walls in gapped bilayer graphene are predicted to host long-lived plasmons with lifetimes 2 orders of magnitude higher than those in single-layer graphene.<sup>15</sup> Recent experiments have shown the tunability of correlated states in twisted double bilayer graphene using a displacement field,<sup>16,17</sup> while twisted trilayer graphene under a displacement field has raised

**Received:** April 25, 2022

**Revised:** July 14, 2022

**Published:** July 25, 2022



the bar of the superconductivity critical temperature in graphene-based systems beyond 2 K.<sup>18,19</sup>

Independent control of carrier density and displacement field is achieved in transport experiments by placing two separately contacted gate electrodes, one on the top and one on the bottom of the sample. This is more difficult in optical experiments, as the top-gate electrode interferes with the optical path. A sufficiently transparent conducting material is therefore needed for the top electrode. Remarkably, the transparency requirement for near-field experiments is even more stringent than for far-field measurements, in particular, those close to the resonances of the structure, as discussed later.

The traditional choice of a top-gate material for 2D material samples is an evaporated gold film. In order to be transparent in the relevant optical range, the electrode thickness must be well-below the skin depth of the material to avoid screening of the near-field electromagnetic field. Typical metals have a skin depth of tens of nanometers for infrared frequencies,<sup>20</sup> which requires the metal film to be only few nanometers thick. Even with metallic films thinner than their skin depth, it is difficult to meet the transparency requirements imposed by near-field experiments, which we carefully quantify in the following. In contrast, conducting oxides, like indium–tin oxide (ITO), are commonly used as transparent electrodes for visible light but are not transparent at infrared frequencies.<sup>21</sup>

Recent experiments<sup>22–24</sup> have made advances in realizing a transparent top gate for s-SNOM experiments with 2D materials, which also provide atomically flat interfaces and allow for easier device integration. Single-layer graphene is sufficiently transparent to probe near-field signals through it,<sup>22</sup> yet its own plasmonic resonance interferes with the optical response of the material underneath, complicating the interpretation of the observed near-field signal.<sup>23,24</sup> Still, for studying structural changes that do not involve collective resonances, this is not an obstacle.<sup>22</sup> As an alternative to graphene, the TMD MoS<sub>2</sub> has been used, which indeed does not host any resonances that disturb the near-field signal.<sup>23</sup> However, since this material is unipolar due to Fermi level pinning at the contacts, it can only introduce p-type doping in the material below.<sup>25</sup>

In this work, we show that WSe<sub>2</sub> can act as an infrared-transparent bipolar gate electrode for near-field experiments as schematically illustrated in Figure 1. We validate its performance by studying the change in induced plasmon wavelength  $\lambda_p$  in bilayer graphene. This allows us to determine the carrier density induced by the top gate, while at the same time we characterize to what extent a charged top layer obstructs the observation of plasmons.

We first rigorously derive the transparency requirement for a top-gate electrode to be used in near-field optical experiments. The near-field response of an homogeneous layered structure is completely determined by its reflection coefficient  $r$  for transverse magnetic (TM) waves (the coupling to transverse-electric modes is negligible in near-field) that is a function of the angular frequency  $\omega$  and the in-plane wavevector  $q$ . Adding another thin layer (either a 2D material or a thin film of a bulk material) on top of the structure alters the reflection coefficient according to eq 1 (see the derivation in section 3 of the Supporting Information):

$$r' = r \frac{1 - S - r^{-1}S}{1 + S + rS} \quad (1)$$

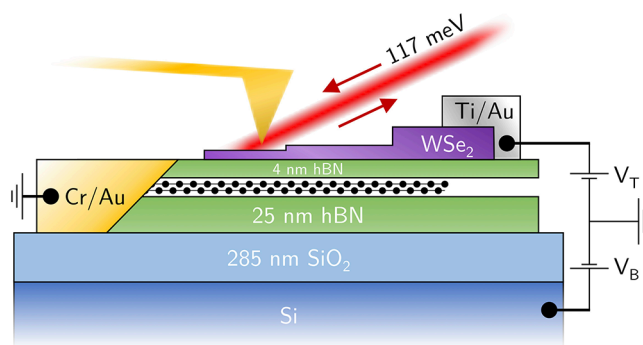


**Figure 1.** Device schematic. Schematic of our near-field experiment carried out on a device consisting of hBN-encapsulated bilayer graphene. By applying a voltage to a staircase flake of WSe<sub>2</sub> (2–6 layers), we tune the carrier density in the bilayer graphene without obstructing the near-field access, as verified by probing the plasmon properties. Together with the silicon bottom gate, this allows full control of the carrier density and displacement field in bilayer graphene.

where  $r'$  is the reflection coefficient (a function of  $\omega$  and  $q$ ) of the structure after the addition of the new layer and  $S$  quantifies the optical disturbance introduced by the new layer (as defined in section 3 of the Supporting Information).  $S$  depends on the optical conductivity of the new layer as

$$S(q, \omega) = \frac{\sigma_{2D}(q, \omega) \sqrt{\omega^2/c^2 - q^2}}{2\epsilon_0\omega} \quad (2)$$

where  $\sigma_{2D}$  is the 2D longitudinal (in the direction of the wavevector) conductivity of the material,  $c$  is the speed of light, and  $\epsilon_0$  is the vacuum permittivity. For 2D materials,  $\sigma_{2D}$  is directly the optical conductivity of the material (in  $\Omega^{-1}$ ), while for thin layers of three-dimensional conducting materials,  $\sigma_{2D} = \sigma\delta$ , where  $\sigma$  is the optical conductivity and  $\delta$  is the thickness of the layer (see the detailed discussion in section 3 of the Supporting Information). We do not consider thick films since their impact on the optical signal is always stronger than that of thin films made of the same material.

Equation 1 shows that the reflection coefficient is not affected by the addition of the new layer ( $r' \approx r$ ) when each of the three conditions  $|S| \ll 1$ ,  $|r|$ , and  $|r|^{-1}$  is satisfied ( $S = -1$  is the resonance condition of the new layer when isolated; our conditions therefore imply the absence of resonances of the new layer). The reflection coefficient can be larger than one in the absolute value when decaying fields are concerned (i.e., when  $q > \omega/c$ ) and peaks exactly at the positions of the collective oscillations,<sup>26</sup> reaching values of the order of the quality factor  $Q$  of the collective oscillation. To observe a collective oscillation without distortion we therefore need  $|S| \ll 1/Q$ .

Figure 2 shows a comparison of the values of  $|S|$  calculated in the ranges of wavevector and frequency that are relevant in typical s-SNOM experiments for single-layer graphene, trilayer WSe<sub>2</sub>, and a 1 nm gold film. Most plasmonic excitations probed in room-temperature s-SNOM experiments have  $Q \approx 10$ . It is therefore not possible to study plasmonic excitations using graphene or gold films as a transparent top gate in the mid-infrared regime. In contrast, trilayer WSe<sub>2</sub> is well-suited for this purpose, at least for photon energies above 100 meV.

The optical disturbance can be reduced by reducing the optical conductivity of the top-gate material, as shown in eq 2.

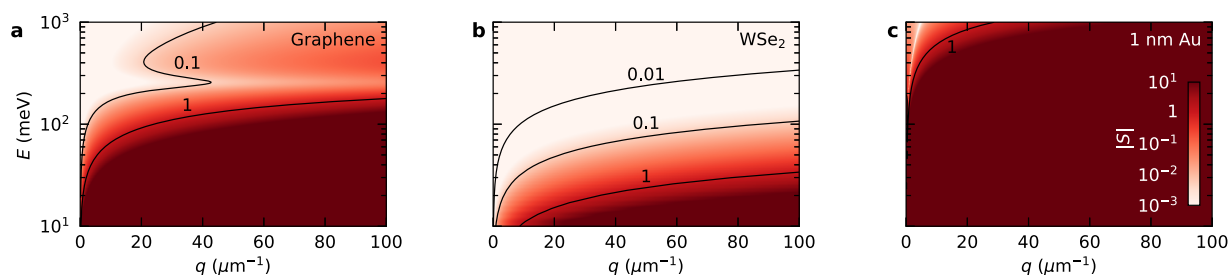


**Figure 2.** Optical disturbance introduced by different top layers. (a) Calculated  $|S|(q, \omega)$  for single-layer graphene with  $n = 2 \times 10^{12} \text{ cm}^{-2}$  and  $\tau = 200 \text{ fs}$  at room temperature. The full nonlocal longitudinal conductivity has been taken into account. The horizontal feature appearing at  $\approx 300 \text{ meV}$  is related to the onset of interband transitions at twice the Fermi energy. (b) Same as panel a for trilayer  $\text{WSe}_2$ , modeled as a Drude conductor with  $n = 2 \times 10^{12} \text{ cm}^{-2}$ ,  $m^* = 1.2 m_e$ ,<sup>27</sup> and  $\tau = 100 \text{ fs}$ .<sup>28</sup> (c) Same as in panel a for a 1 nm thick gold film. The permittivity of gold is taken from ref 29.

For a material with a Drude-like response, this can be done by reducing the carrier density and the relaxation time or by increasing the effective mass. The carrier density changes when the gate voltage is applied, and for effective gating, it cannot be smaller than  $\approx 10^{12} \text{ cm}^{-2}$ . Additionally, the scattering time  $\tau$  is typically too long to play a role for mid-infrared frequencies. The search for better materials for top gating should therefore be oriented toward materials with larger effective masses.

$\text{WSe}_2$  can be exfoliated down to a single layer<sup>30,31</sup> of 0.7 nm and has relatively low mobilities up to  $500 \text{ cm}^2/(\text{V s})$ .<sup>28,30</sup> In contrast to  $\text{MoS}_2$ ,  $\text{WSe}_2$  is ambipolar, and its carrier concentration can be tuned electrostatically all the way from n-type (electrons) to p-type (holes).<sup>32</sup> A common issue arising with TMDs is the Schottky barrier forming at the metal–semiconductor interface, typically by severely blocking transport through either the valence or conduction band. This can be overcome by a suitable choice of two different metals for the source and drain contacts.<sup>33</sup> However, since we intend to use  $\text{WSe}_2$  solely as a gate electrode, a highly resistive contact does not pose an issue, provided we do not modulate the carrier density at high frequencies. On the basis of an estimated device resistance<sup>34</sup> of  $\approx 40 \text{ k}\Omega$  and a geometrical capacitance of  $\approx 0.8 \text{ pF}$ , we obtain an RC cutoff frequency of  $\approx 200 \text{ MHz}$ .

Figure 1 shows a schematic of the dual-gated device used in this experiment using  $\text{WSe}_2$  as top gate. Our device consists of bilayer graphene (BLG) encapsulated in hexagonal boron nitride (hBN) with a thin  $\text{WSe}_2$  staircase flake acting as a top gate, fabricated as described in section 1 of the Supporting Information. Given the rapid decay of the near-field signal in the out-of-plane direction, we use a 4 nm thin top hBN flake. The Si/SiO<sub>2</sub> bottom gate serves as a back gate to bring BLG into a highly doped state where plasmons do not suffer from Landau damping.<sup>9</sup> In addition, the bottom gate provides a reference for determining the plasmon wavelength  $\lambda_p$  as a function of the induced carrier density  $n$ . Over the course of 2 months, we did not observe any signs of degradation of the  $\text{WSe}_2$ , despite carrying out the experiments in ambient conditions.<sup>35</sup>

Figure 3a shows a near-field image of BLG with doping  $n \sim 10^{13} \text{ cm}^{-2}$  induced by the bottom gate at  $V_B = 80 \text{ V}$  along with photodoping, but with  $V_T = 0$ . Photodoping involves photoexciting defect states at the SiO<sub>2</sub>/hBN interface,<sup>8,36</sup> which effectively sets the charge-neutrality point  $V_D$  at  $-65 \text{ V}$ , as extracted from the maximum of the measured source-drain resistance. The fringes running parallel to the BLG edge are a manifestation of plasmon polaritons, which we observe as both tip-launched, edge-reflected ( $\lambda_p/2$  period) and edge-launched

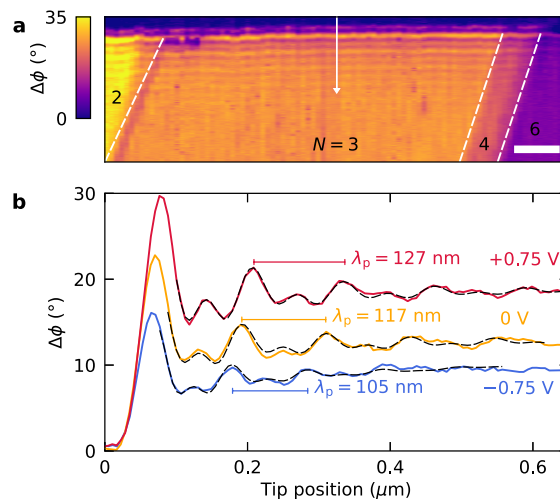


**Figure 3.** Controlling the plasmon wavelength with a  $\text{WSe}_2$  top gate. (a) Spatial map of the near-field phase contrast at the edge of the bilayer graphene, corresponding to the yellow box in Figure S1. The silicon bottom gate induces a high carrier density of  $\sim 10^{13} \text{ cm}^{-2}$  ( $V_B - V_D = 145 \text{ V}$ ), allowing the propagation of plasmon polaritons, as seen by the fringes running parallel to the edge. The area shown is covered by  $\text{WSe}_2$  of various thicknesses, as indicated by the number of layers  $N$ . The excitation energy is 117 meV, and the scale bar is 300 nm. (b) Line cuts along the white arrow in panel (a) demonstrate the effect of the  $\text{WSe}_2$  top gate while keeping  $V_B - V_D = 145 \text{ V}$ . Without obstructing near-field access, applying a voltage to  $\text{WSe}_2$  alters the carrier density in BLG ( $V_T$  indicated for each line cut), which affects the measured plasmon wavelength  $\lambda_p$  as extracted from a fit (black dashed lines).

( $\lambda_p$  period),<sup>9</sup> as explained in section 2 of the Supporting Information.

As a next step, we apply a voltage  $V_T$  on the  $\text{WSe}_2$  top gate while keeping BLG in the same highly doped state, and we record the near-field signal along the arrow in Figure 3a. At this location, the top gate consists of three layers of  $\text{WSe}_2$  with a total thickness of  $\approx 2.2 \text{ nm}$ . Figure 3b demonstrates that by applying a voltage to the top gate we are able to change the observed plasmon wavelength. By fitting the oscillations to the model introduced in section 2 of the Supporting Information, we determine the change in plasmon wavelength to be  $\pm 10 \text{ nm}$  for  $V_T = \pm 0.75 \text{ V}$ . In addition, the signal-to-noise ratio of the near-field signal stays qualitatively constant while changing the top-gate voltage, confirming that the presence of the top gate does not affect the optical signal.



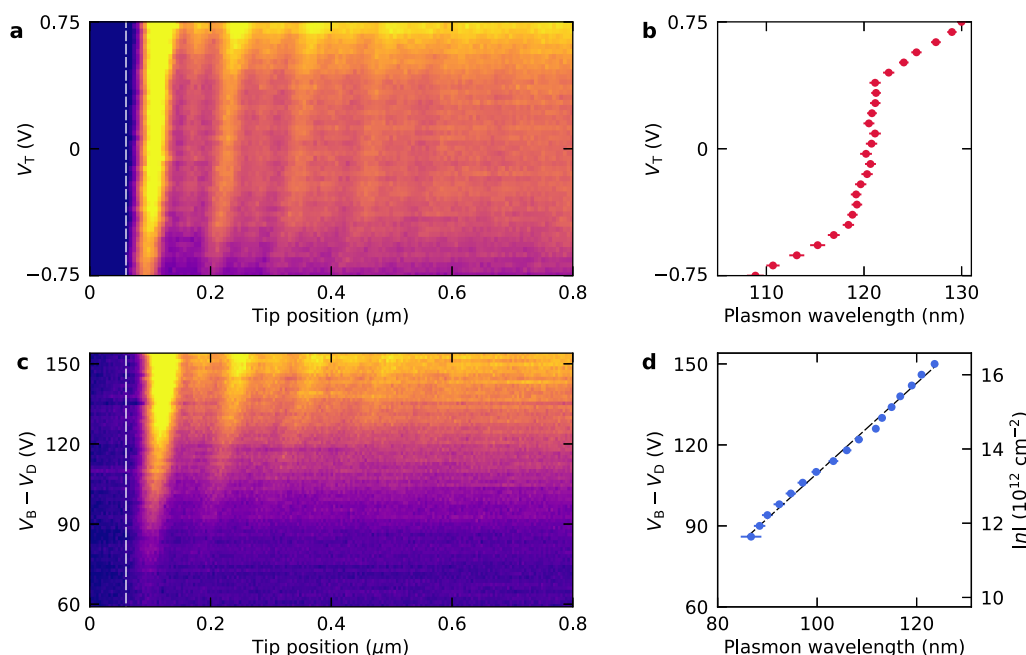


**Figure 4.** Systematically measuring the response of the WSe<sub>2</sub> top gate. (a) Line cut of the near-field phase signal along the white arrow in Figure 3a for a range of top-gate voltages, while  $V_B - V_D = 145$  V. The edge of bilayer graphene is marked with a dashed line. The color scale is the same as in Figure 3a, covering an 18° phase difference. (b) The extracted plasmon wavelength shows a piece-wise linear dependence on the top-gate voltage. The error bars represent  $\pm 1\sigma$ . (c) Near-field phase signal along the same line as panel a for a range of bottom gate voltages ( $V_T = 0$  V), serving as calibration to determine the carrier density induced by the WSe<sub>2</sub> top gate. (d) The extracted plasmon wavelength scales approximately linearly with the bottom gate voltage and carrier density, as indicated by a linear fit (dashed line).

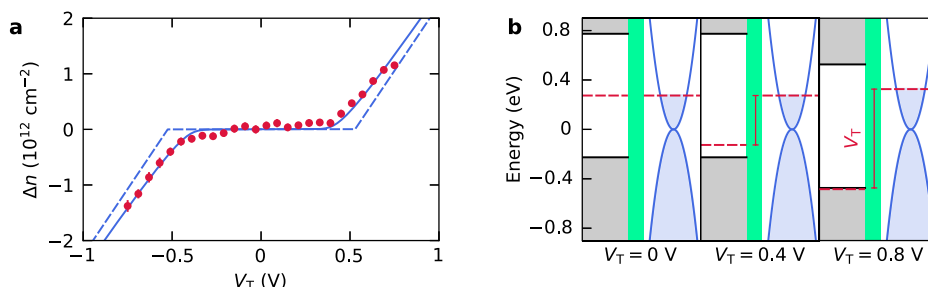


**Figure 5.** Gating efficiency of trilayer WSe<sub>2</sub> and band alignment. (a) Induced shift in the carrier density  $\Delta n$  in BLG by applying a voltage to WSe<sub>2</sub> through a 4 nm hBN layer. The flat response for small top-gate voltages ( $|V_T| < 0.4$  V) arises from the intrinsic gap in WSe<sub>2</sub>. For larger voltages ( $|V_T| > 0.4$  V), WSe<sub>2</sub> acts as a conductor, and the slope is determined by the geometric capacitance. From a fit according to the electrostatic model with  $T = 300$  K, we extract a gap of 1.05 eV in WSe<sub>2</sub> (solid line). The dashed line represents the calculated  $\Delta n$  at zero temperature using the same fit parameters. (b) Band alignment of semiconducting WSe<sub>2</sub> (gray bands) with respect to BLG (blue bands) for three different positive top-gate voltages. For small  $V_T$ , the chemical potential of WSe<sub>2</sub> shifts down by  $V_T$  (middle panel). Once  $V_T$  is large enough that the chemical potential of WSe<sub>2</sub> reaches the valence band edge, carriers are injected into BLG, moving its chemical potential upward (right panel). At the same time, the bands of WSe<sub>2</sub> and BLG are shifted apart such that the  $V_T$  equals the difference in chemical potentials, indicated by the vertical bar.

To study the response of the transparent top gate in more detail, we measure the near-field signal while systematically scanning the voltage on the top gate, shown in Figure 4a. Judging by the fringe spacing for different  $V_T$ , these data suggest that the top gate only becomes “active” for high  $|V_T|$ . To examine this quantitatively, we fit the data to the function reported in section 2 of the Supporting Information for each voltage, and we extract the plasmon wavelength as a function of the top-gate voltage (Figure 4b). We find indeed a piece-wise linear function with an inactive region for low  $|V_T|$ , while the slope of  $\lambda_p(V_T)$  is rather similar for  $|V_T| > 0.4$  V.

To understand the peculiar shape of  $\lambda_p(V_T)$  from a perspective of the electrostatics in our device, we first need to determine the induced carrier density in BLG by the WSe<sub>2</sub> top gate. To do so, we calibrate  $\lambda_p(n)$  by using the bottom gate

as a reference. According to eq 3 introduced below, when  $V_T = 0$  V the induced carrier density can be described by a simple parallel plate capacitor only dependent on  $V_B$ . We measure the plasmon fringes along the same line cut while varying the voltage on the bottom gate and keeping  $V_T = 0$  V (Figure 4c,d). Applying the same fitting procedure at each voltage point, we find a linear dependence of the plasmon wavelength on  $V_B$ , as is expected for a 2D conductor with parabolic bands.<sup>37</sup> Using the capacitance of the bottom gate as mentioned below and  $V_D = -74$  V in this measurement, we can convert voltages to carrier densities and fit the plasmon wavelength (Figure 4d.) to a linear relation  $\lambda_p = an + b$ , yielding  $a = 8.23 \times 10^{-12}$  nm cm<sup>2</sup> and  $b = 34.5$  nm. From this calibration, we can convert the measured change in plasmon wavelength (Figure 4b) to the carrier density  $\Delta n$  induced by

the WSe<sub>2</sub> top gate. The final result of our experiment is shown Figure 5a that displays the carrier density induced by the gate as a function of the top-gate voltage. These measurements were obtained in a completely optical way without relying on transport measurements on graphene. This demonstrates that graphene plasmons can act as independent local probes of the carrier density that can complement traditional transport measurements.

We can understand our results in terms of a simple model that relates the carrier density  $n$  in BLG for given gate voltages  $V_B$  and  $V_T$ . This is based on the equilibrium of the electrochemical potentials (see the derivation in section 5 of the Supporting Information) and leads to the relation

$$n = \frac{C_B(V_B - V_D)}{e} + \frac{C_T V_T}{e} + \frac{C_T \Delta\mu_{\text{WSe}_2}(V_T)}{e^2} \quad (3)$$

where  $C_T \approx 7.7 \text{ mF/m}^2$  and  $C_B \approx 0.12 \text{ mF/m}^2$  are the geometric capacitances corresponding to the top and bottom gate,  $e$  is the unit charge,  $\Delta\mu_{\text{WSe}_2}$  is the shift in chemical potential of WSe<sub>2</sub> with respect to its value at  $V_T = 0 \text{ V}$ , and the quantum capacitance of BLG  $C_Q \approx 62 \text{ mF/m}^2$  has been ignored since it is much larger than  $C_{T/B}$ . From this equation, we see that for  $V_T = 0 \text{ V}$ , the carrier density in BLG can be described by the geometric capacitance of the bottom gate (first term), which we used above for the calibration of  $\lambda_p(n)$ . However, once we fix  $V_B$ , the change in carrier density is determined by the geometric capacitance of the top gate (second term) and the quantum capacitance of WSe<sub>2</sub> (last term). The interplay of the last two terms causes the steplike behavior seen in Figure 5a, with the central flat region corresponding to the values of  $V_T$  for which the chemical potential falls deep in the gap of the semiconductor. However, while the carrier type in WSe<sub>2</sub> changes from electrons to holes while scanning  $V_T$ , the BLG remains electron-doped due to the large density offset induced by the combination of bottom gate voltage and photodoping. The calculation of  $\Delta\mu_{\text{WSe}_2}(V_T)$  is presented in section 5 of the Supporting Information.

A band alignment diagram of WSe<sub>2</sub> and BLG explains the gating response in more detail (Figure 5b). Starting with a BLG at a high carrier density induced by the bottom gate, the chemical potentials of WSe<sub>2</sub> and BLG are aligned for  $V_T = 0 \text{ V}$ . In this situation, the chemical potential of WSe<sub>2</sub> resides within the energy gap of WSe<sub>2</sub>. Upon increasing  $V_T$ , owing to the low quantum capacitance of WSe<sub>2</sub> in its insulating state,  $\Delta\mu_{\text{WSe}_2}$  shifts down by  $V_T$  until it reaches the valence band. Once that happens, holes are introduced in the valence band, and the capacitively induced electrons in BLG shift the chemical potential of BLG upward. Due to the relatively high density of states of the valence band of WSe<sub>2</sub>, its chemical potential remains close to the valence band edge for higher carrier densities. Since the difference in chemical potential between WSe<sub>2</sub> and BLG has to be equal to  $V_T$ , the bands of WSe<sub>2</sub> and BLG separate in energy for higher carrier densities.

In fitting the data to our model in Figure 5a, we only leave the valence and conduction band energies as free fit parameters, while the other parameters can be estimated with sufficient accuracy. The fit yields a band gap of  $(1.05 \pm 0.02) \text{ eV}$  (the error being estimated from the fitting procedure) and is almost perfectly centered at  $V_T = 0 \text{ V}$ . We theoretically calculated the electronic band gap and the densities of states at the band extrema of our material by carrying out density functional theory (DFT) calculations for trilayer WSe<sub>2</sub> using

the Atomic Simulations Recipe environment and the GPAW package.<sup>38,39</sup> The electronic band structure and the densities of the states are reported in the section 4 of the Supporting Information. We find an electronic band gap of 1.05 eV which agrees very well with the experimental results in this work and previous theoretical calculations.<sup>27,40,41</sup> The agreement with the experiment is surprising because DFT is known to underestimate the band gaps, and generally, the experimental band gap of trilayer WSe<sub>2</sub> is reported<sup>27,42,43</sup> at higher values around 1.45 eV. We believe that this discrepancy is caused by the charge imbalance present in WSe<sub>2</sub> when generating an external electric field. The internal field due to the charge imbalance can modify the electronic bands and is expected to reduce the gap size due to band bending.

In summary, we have shown that few-layer WSe<sub>2</sub> can be used as a transparent ambipolar top gate for near-field experiments. This is demonstrated by tuning the plasmonic excitations in bilayer graphene via a WSe<sub>2</sub> top gate without obscuring the near-field scattering signal. Nanoscale measurements of the plasmon wavelength allow us to extract the gating efficiency, which we capture in a minimal model that considers the geometric and quantum capacitances. We expect other members of the TMD class, in particular those with higher effective masses, to be equally suitable as infrared-transparent top gates due to their similarity, while their scalability via CVD growth allows for easy device integration.<sup>44–47</sup> This work paves the way for future cryogenic near-field experiments on exotic states in dual-gated sample geometries.<sup>15–19</sup> In contrast, our experiment allowed to directly probe the energy gap and band-alignment (relative to graphene) of semiconducting 2D materials, providing information that can complement the data obtained by other techniques.<sup>48</sup>

## METHODS

**Measurement Details.** The near-field measurements have been carried out on the neaSNOM platform (neaspec), equipped with a CO<sub>2</sub> gas laser (Access Laser) and a fast HgCdTe detector (Kolmar Technologies). We focus 15 mW of infrared light (wavelength 10.6  $\mu\text{m}$ , corresponding to a photon energy of 117 meV) onto a PtIr-coated AFM tip (Nanoworld), which oscillates at a frequency of  $\approx 250 \text{ kHz}$  with a tapping amplitude of 80–100 nm. We operate the system in a pseudoheterodyne mode<sup>49</sup> using a ZnSe beam splitter to obtain the phase resolved near-field signal. To avoid detecting unwanted far-field signals, we record the near-field signal at the third harmonic of the cantilever oscillation. All measurements are carried out in ambient conditions.

## ASSOCIATED CONTENT

### Supporting Information

The Supporting Information is available free of charge at <https://pubs.acs.org/doi/10.1021/acs.nanolett.2c01658>.

Device fabrication and geometry, extraction of plasmon wavelength, reflection perturbation induced by an additional layer, energy band structure of WSe<sub>2</sub>, and carrier density in graphene as a function of the top and bottom gate voltages (PDF)

## AUTHOR INFORMATION

### Corresponding Authors

Iacopo Torre – ICFO-Institut de Ciències Fotòniques, The Barcelona Institute of Science and Technology, 08860

Castelldefels, Barcelona, Spain; [orcid.org/0000-0001-6515-181X](https://orcid.org/0000-0001-6515-181X); Email: [iacopo.torre@icfo.eu](mailto:iacopo.torre@icfo.eu)

**Frank H. L. Koppens** – ICFO-Institut de Ciències Fotòniques, The Barcelona Institute of Science and Technology, 08860 Castelldefels, Barcelona, Spain; ICREA-Institució Catalana de Recerca i Estudis Avançats, 08010 Barcelona, Spain; [orcid.org/0000-0001-9764-6120](https://orcid.org/0000-0001-9764-6120); Email: [frank.koppens@icfo.eu](mailto:frank.koppens@icfo.eu)

## Authors

**Niels C. H. Hesp** – ICFO-Institut de Ciències Fotòniques, The Barcelona Institute of Science and Technology, 08860 Castelldefels, Barcelona, Spain; [orcid.org/0000-0001-8111-9780](https://orcid.org/0000-0001-8111-9780)

**Mark Kamper Svendsen** – CAMD, Computational Atomic-Scale Materials Design, Department of Physics, Technical University of Denmark, DK-2800 Kongens Lyngby, Denmark; [orcid.org/0000-0001-9718-849X](https://orcid.org/0000-0001-9718-849X)

**Kenji Watanabe** – Research Center for Functional Materials, National Institute for Materials Science, Tsukuba 305-0044, Japan; [orcid.org/0000-0003-3701-8119](https://orcid.org/0000-0003-3701-8119)

**Takashi Taniguchi** – International Center for Materials Nanoarchitectonics, National Institute for Materials Science, Tsukuba 305-0044, Japan; [orcid.org/0000-0002-1467-3105](https://orcid.org/0000-0002-1467-3105)

**Kristian S. Thygesen** – CAMD, Computational Atomic-Scale Materials Design, Department of Physics, Technical University of Denmark, DK-2800 Kongens Lyngby, Denmark; Center for Nanostructured Graphene (CNG), Department of Physics, Technical University of Denmark, DK-2800 Kongens Lyngby, Denmark; [orcid.org/0000-0001-5197-214X](https://orcid.org/0000-0001-5197-214X)

Complete contact information is available at: <https://pubs.acs.org/10.1021/acs.nanolett.2c01658>

## Author Contributions

N.C.H.H. and F.H.L.K. conceived the experiment. N.C.H.H. fabricated the devices and carried out the experiments. K.W. and T.T. synthesized the hBN crystals. I.T. developed the theoretical modeling of the experiment. M.K.S. and K.S.T. carried out the DFT band-structure calculations. N.C.H.H., I.T. and F.H.L.K. analyzed the results and wrote the manuscript with input from all the authors. F.H.L.K. supervised the work.

## Notes

The data that support the plots within this paper and other findings of this study are available from the corresponding author upon reasonable request.

The authors declare no competing financial interest.

## ACKNOWLEDGMENTS

F.H.L.K. acknowledges financial support from the Government of Catalonia through the SGR grant, from the Spanish Ministry of Economy and Competitiveness through the Severo Ochoa Programme for Centres of Excellence in R&D (ref. SEV-2015-0522), and from Explora Ciencia (ref. FIS2017-91599-EXP). F.H.L.K. also acknowledges support by Fundacio Cellex Barcelona, Generalitat de Catalunya through the CERCA program, the Mineco grant Plan Nacional (ref. FIS2016-81044-P), and the Agency for Management of University and Research Grants (AGAUR) (ref. 2017-SGR-1656). Furthermore, the research leading to these results has received funding

from the European Union's Horizon 2020 programme under grant agreement refs. 785219 (Graphene Flagship Core2), 881603 (Graphene Flagship Core3), and 820378 (Quantum Flagship). This work was supported by the ERC TOP-ONANOP under grant agreement ref. 726001. N.C.H.H. acknowledges funding from the European Union's Horizon 2020 research and innovation programme under the Marie Skłodowska-Curie grant agreement ref. 665884. I.T. acknowledges funding from the Spanish Ministry of Science, Innovation and Universities (MCIU), and the State Research Agency (AEI) via the Juan de la Cierva fellowship ref. FJC2018-037098-I. K.W. and T.T. acknowledge support from JSPS KAKENHI (Grant Numbers 19H05790, 20H00354, and 21H05233). K.S.T. acknowledges funding from the European Research Council (ERC) Grant No. 773122 (LIMA). K.S.T. is a Villum Investigator supported by VILLUM FONDEN (grant no. 37789).

## REFERENCES

- (1) Novotny, L.; Stranick, S. J. Near-field optical microscopy and spectroscopy with pointed probes. *Annu. Rev. Phys. Chem.* **2006**, *57*, 303–331.
- (2) Chen, J.; Badioli, M.; Alonso-González, P.; Thongrattanasiri, S.; Huth, F.; Osmond, J.; Spasenović, M.; Centeno, A.; Pesquera, A.; Godignon, P.; Zurutuza Elorza, A.; Camara, N.; de Abajo, F. J. G.; Hillenbrand, R.; Koppens, F. H. L. Optical nano-imaging of gate-tunable graphene plasmons. *Nature* **2012**, *487*, 77–81.
- (3) Fei, Z.; Rodin, A. S.; Andreev, G. O.; Bao, W.; McLeod, A. S.; Wagner, M.; Zhang, L. M.; Zhao, Z.; Thiemens, M.; Dominguez, G.; Fogler, M. M.; Neto, A. H. C.; Lau, C. N.; Keilmann, F.; Basov, D. N. Gate-tuning of graphene plasmons revealed by infrared nano-imaging. *Nature* **2012**, *487*, 82–85.
- (4) Dai, S.; et al. Tunable Phonon Polaritons in Atomically Thin van der Waals Crystals of Boron Nitride. *Science* **2014**, *343*, 1125–1129.
- (5) Basov, D. N.; Asenjo-Garcia, A.; Schuck, P. J.; Zhu, X.; Rubio, A. Polariton panorama. *Nanophotonics* **2020**, *10*, 549–577.
- (6) Basov, D. N.; Fogler, M. M.; Garcia de Abajo, F. J. Polaritons in van der Waals materials. *Science* **2016**, *354*, aag1992.
- (7) Low, T.; Chaves, A.; Caldwell, J. D.; Kumar, A.; Fang, N. X.; Avouris, P.; Heinz, T. F.; Guinea, F.; Martin-Moreno, L.; Koppens, F. Polaritons in layered two-dimensional materials. *Nat. Mater.* **2017**, *16*, 182–194.
- (8) Woessner, A.; Alonso-Gonzalez, P.; Lundberg, M. B.; Gao, Y.; Barrios-Vargas, J. E.; Navickaite, G.; Ma, Q.; Janner, D.; Watanabe, K.; Cummings, A. W.; et al. Near-field photocurrent nanoscopy on bare and encapsulated graphene. *Nat. Commun.* **2016**, *7*, 10783.
- (9) Woessner, A.; Lundberg, M. B.; Gao, Y.; Principi, A.; Alonso-González, P.; Carrega, M.; Watanabe, K.; Taniguchi, T.; Vignale, G.; Polini, M.; Hone, J.; Hillenbrand, R.; Koppens, F. H. L. Highly confined low-loss plasmons in graphene–boron nitride heterostructures. *Nat. Mater.* **2015**, *14*, 421–425.
- (10) Ni, G. X.; McLeod, A. S.; Sun, Z.; Wang, L.; Xiong, L.; Post, K. W.; Sunku, S. S.; Jiang, B.-Y.; Hone, J.; Dean, C. R.; Fogler, M. M.; Basov, D. N. Fundamental limits to graphene plasmonics. *Nature* **2018**, *557*, 530–533.
- (11) Lundberg, M. B.; Gao, Y.; Asgari, R.; Tan, C.; Van Duppen, B.; Autore, M.; Alonso-González, P.; Woessner, A.; Watanabe, K.; Taniguchi, T.; Hillenbrand, R.; Hone, J.; Polini, M.; Koppens, F. H. L. Tuning quantum nonlocal effects in graphene plasmonics. *Science* **2017**, *357*, 187–191.
- (12) Sunku, S. S.; Ni, G. X.; Jiang, B. Y.; Yoo, H.; Sternbach, A.; McLeod, A. S.; Stauber, T.; Xiong, L.; Taniguchi, T.; Watanabe, K.; Kim, P.; Fogler, M. M.; Basov, D. N. Photonic crystals for nano-light in moiré graphene superlattices. *Science* **2018**, *362*, 1153–1156.
- (13) Schmidt, P.; Vialla, F.; Latini, S.; Massicotte, M.; Tielrooij, K.-J.; Mastel, S.; Navickaite, G.; Danovich, M.; Ruiz-Tijerina, D. A.; Yelgel, C.; Fa'ko, V.; Thygesen, K. S.; Hillenbrand, R.; Koppens, F.



- H. L. Nano-imaging of intersubband transitions in van der Waals quantum wells. *Nat. Nanotechnol.* **2018**, *13*, 1035–1041.
- (14) McCann, E.; Koshino, M. The electronic properties of bilayer graphene. *Rep. Prog. Phys.* **2013**, *76*, 056503.
- (15) Hasdeo, E. H.; Song, J. C. W. Long-Lived Domain Wall Plasmons in Gapped Bilayer Graphene. *Nano Lett.* **2017**, *17*, 7252–7257.
- (16) Liu, X.; Hao, Z.; Khalaf, E.; Lee, J. Y.; Ronen, Y.; Yoo, H.; Haei Najafabadi, D.; Watanabe, K.; Taniguchi, T.; Vishwanath, A.; Kim, P. Tunable spin-polarized correlated states in twisted double bilayer graphene. *Nature* **2020**, *583*, 221–225.
- (17) Cao, Y.; Rodan-Legrain, D.; Rubies-Bigorda, O.; Park, J. M.; Watanabe, K.; Taniguchi, T.; Jarillo-Herrero, P. Tunable correlated states and spin-polarized phases in twisted bilayer–bilayer graphene. *Nature* **2020**, *583*, 215–220.
- (18) Park, J. M.; Cao, Y.; Watanabe, K.; Taniguchi, T.; Jarillo-Herrero, P. Tunable strongly coupled superconductivity in magic-angle twisted trilayer graphene. *Nature* **2021**, *590*, 249–255.
- (19) Hao, Z.; Zimmerman, A. M.; Ledwith, P.; Khalaf, E.; Najafabadi, D. H.; Watanabe, K.; Taniguchi, T.; Vishwanath, A.; Kim, P. Electric field–tunable superconductivity in alternating-twist magic-angle trilayer graphene. *Science* **2021**, *371*, 1133–1138.
- (20) Rahman, F. *Nanostructures in Electronics and Photonics*; Jenny Stanford Publishing: New York, 2008; pp 1–316.
- (21) Amalric-Popescu, D.; Bozon-Verduraz, F. Infrared studies on SnO<sub>2</sub> and Pd/SnO<sub>2</sub>. *Catal. Today* **2001**, *70*, 139–154.
- (22) Li, H.; Utama, M. I. B.; Wang, S.; Zhao, W.; Zhao, S.; Xiao, X.; Jiang, Y.; Jiang, L.; Taniguchi, T.; Watanabe, K.; Weber-Bargioni, A.; Zettl, A.; Wang, F. Global Control of Stacking-Order Phase Transition by Doping and Electric Field in Few-Layer Graphene. *Nano Lett.* **2020**, *20*, 3106–3112.
- (23) Sunku, S. S.; Halbertal, D.; Engelke, R.; Yoo, H.; Finney, N. R.; Curreli, N.; Ni, G.; Tan, C.; McLeod, A. S.; Lo, C. F. B.; Dean, C. R.; Hone, J. C.; Kim, P.; Basov, D. N. Dual-Gated Graphene Devices for Near-Field Nano-imaging. *Nano Lett.* **2021**, *21*, 1688–1693.
- (24) Luo, W.; Kuzmenko, A. B.; Qi, J.; Zhang, N.; Wu, W.; Ren, M.; Zhang, X.; Cai, W.; Xu, J. Nanoinfrared Characterization of Bilayer Graphene Conductivity under Dual-Gate Tuning. *Nano Lett.* **2021**, *21*, 5151–5157.
- (25) Kim, C.; Moon, I.; Lee, D.; Choi, M. S.; Ahmed, F.; Nam, S.; Cho, Y.; Shin, H.-J.; Park, S.; Yoo, W. J. Fermi Level Pinning at Electrical Metal Contacts of Monolayer Molybdenum Dichalcogenides. *ACS Nano* **2017**, *11*, 1588–1596.
- (26) Gonçalves, P. A. D.; Peres, N. M. R. *An Introduction to Graphene Plasmonics*; World Scientific: Singapore, 2016.
- (27) Movva, H. C.; Lovorn, T.; Fallahazad, B.; Larentis, S.; Kim, K.; Taniguchi, T.; Watanabe, K.; Banerjee, S. K.; MacDonald, A. H.; Tutuc, E. Tunable  $\Gamma$ -K Valley Populations in Hole-Doped Trilayer WSe<sub>2</sub>. *Phys. Rev. Lett.* **2018**, *120*, 107703.
- (28) Movva, H. C. P.; Rai, A.; Kang, S.; Kim, K.; Fallahazad, B.; Taniguchi, T.; Watanabe, K.; Tutuc, E.; Banerjee, S. K. High-Mobility Holes in Dual-Gated WSe<sub>2</sub> Field-Effect Transistors. *ACS Nano* **2015**, *9*, 10402–10410.
- (29) Johnson, P. B.; Christy, R. W. Optical Constants of the Noble Metals. *Phys. Rev. B* **1972**, *6*, 4370–4379.
- (30) Podzorov, V.; Gershenson, M. E.; Kloc, C.; Zeis, R.; Bucher, E. High-mobility field-effect transistors based on transition metal dichalcogenides. *Appl. Phys. Lett.* **2004**, *84*, 3301–3303.
- (31) Fang, H.; Chuang, S.; Chang, T. C.; Takei, K.; Takahashi, T.; Javey, A. High-Performance Single Layered WSe<sub>2</sub> p-FETs with Chemically Doped Contacts. *Nano Lett.* **2012**, *12*, 3788–3792.
- (32) Wang, Z.; Li, Q.; Chen, Y.; Cui, B.; Li, Y.; Besenbacher, F.; Dong, M. The ambipolar transport behavior of WSe<sub>2</sub> transistors and its analogue circuits. *NPG Asia Materials* **2018**, *10*, 703–712.
- (33) Das, S.; Appenzeller, J. WSe<sub>2</sub> field effect transistors with enhanced ambipolar characteristics. *Appl. Phys. Lett.* **2013**, *103*, 103501.
- (34) Chuang, H.-J.; Chamlain, B.; Koehler, M.; Perera, M. M.; Yan, J.; Mandrus, D.; Tománek, D.; Zhou, Z. Low-Resistance 2D/2D Ohmic Contacts: A Universal Approach to High-Performance WSe<sub>2</sub>, MoS<sub>2</sub>, and MoSe<sub>2</sub> Transistors. *Nano Lett.* **2016**, *16*, 1896–1902.
- (35) Gammelgaard, L.; Whelan, P. R.; Booth, T. J.; Bøggild, P. Long-term stability and tree-ring oxidation of WSe<sub>2</sub> using phase-contrast AFM. *Nanoscale* **2021**, *13*, 19238–19246.
- (36) Ju, L.; Velasco, J.; Huang, E.; Kahn, S.; Nosioglia, C.; Tsai, H.-Z.; Yang, W.; Taniguchi, T.; Watanabe, K.; Zhang, Y.; Zhang, G.; Crommie, M.; Zettl, A.; Wang, F. Photoinduced doping in heterostructures of graphene and boron nitride. *Nat. Nanotechnol.* **2014**, *9*, 348–352.
- (37) Low, T.; Guinea, F.; Yan, H.; Xia, F.; Avouris, P. Novel Midinfrared Plasmonic Properties of Bilayer Graphene. *Phys. Rev. Lett.* **2014**, *112*, 116801.
- (38) Gjerding, M.; Skovhus, T.; Rasmussen, A.; Bertoldo, F.; Larsen, A. H.; Mortensen, J. J.; Thygesen, K. S. Atomic Simulation Recipes: A Python framework and library for automated workflows. *Comput. Mater. Sci.* **2021**, *199*, 110731.
- (39) Enkovaara, J.; Rostgaard, C.; Mortensen, J. J.; Chen, J.; Dulak, M.; Ferrighi, L.; Gavnholt, J.; Glinvad, C.; Haikola, V.; Hansen, H. A.; et al. Electronic structure calculations with GPAW: a real-space implementation of the projector augmented-wave method. *J. Phys.: Condens. Matter* **2010**, *22*, 253202.
- (40) Dai, X.; Li, W.; Wang, T.; Wang, X.; Zhai, C. Bandstructure modulation of two-dimensional WSe<sub>2</sub> by electric field. *J. Appl. Phys.* **2015**, *117*, 084310.
- (41) Javaid, M.; Russo, S. P.; Kalantar-Zadeh, K.; Greentree, A. D.; Drumm, D. W. Band structure and giant Stark effect in two-dimensional transition-metal dichalcogenides. *Electronic Structure* **2019**, *1*, 015005.
- (42) Zhao, W.; Ghorannevis, Z.; Chu, L.; Toh, M.; Kloc, C.; Tan, P.-H.; Eda, G. Evolution of Electronic Structure in Atomically Thin Sheets of WS<sub>2</sub> and WSe<sub>2</sub>. *ACS Nano* **2013**, *7*, 791–797.
- (43) Zeng, H.; Liu, G.-B.; Dai, J.; Yan, Y.; Zhu, B.; He, R.; Xie, L.; Xu, S.; Chen, X.; Yao, W.; Cui, X. Optical signature of symmetry variations and spin-valley coupling in atomically thin tungsten dichalcogenides. *Sci. Rep.* **2013**, *3*, 1608.
- (44) Lin, Y.-C.; Lu, N.; Perea-Lopez, N.; Li, J.; Lin, Z.; Peng, X.; Lee, C. H.; Sun, C.; Calderin, L.; Browning, P. N.; Bresnehan, M. S.; Kim, M. J.; Mayer, T. S.; Terrones, M.; Robinson, J. A. Direct Synthesis of van der Waals Solids. *ACS Nano* **2014**, *8*, 3715–3723.
- (45) Wang, X.; Gong, Y.; Shi, G.; Chow, W. L.; Keyshar, K.; Ye, G.; Vajtai, R.; Lou, J.; Liu, Z.; Ringe, E.; Tay, B. K.; Ajayan, P. M. Chemical Vapor Deposition Growth of Crystalline Monolayer MoSe<sub>2</sub>. *ACS Nano* **2014**, *8*, 5125–5131.
- (46) Eichfeld, S. M.; et al. Highly Scalable, Atomically Thin WSe<sub>2</sub> Grown via Metal–Organic Chemical Vapor Deposition. *ACS Nano* **2015**, *9*, 2080–2087.
- (47) Liu, B.; Fathi, M.; Chen, L.; Abbas, A.; Ma, Y.; Zhou, C. Chemical Vapor Deposition Growth of Monolayer WSe<sub>2</sub> with Tunable Device Characteristics and Growth Mechanism Study. *ACS Nano* **2015**, *9*, 6119–6127.
- (48) Gutiérrez-Lezama, I.; Ubrig, N.; Ponomarev, E.; Morpurgo, A. F. Ionic gate spectroscopy of 2D semiconductors. *Nature Reviews Physics* **2021**, *3*, 508.
- (49) Ocelic, N.; Huber, A.; Hillenbrand, R. Pseudoheterodyne detection for background-free near-field spectroscopy. *Appl. Phys. Lett.* **2006**, *89*, 101124.